Low-temperature fabrication and characterization of a symmetric hybrid organic–inorganic slab waveguide for evanescent light microscopy

Citation for the original published paper (version of record):

Agnarsson, B., Mapar, M., Sjöberg, M. et al (2018). Low-temperature fabrication and characterization of a symmetric hybrid organic–inorganic slab waveguide for evanescent light microscopy. Nano Futures, 2(2). http://dx.doi.org/10.1088/2399-1984/aac25d

IOP Publishing Nano Futures 2 (2018) 025007 https://doi.org/10.1088/2399-1984/aac25d

NANO FUTURES

OPEN ACCESS

RECEIVED
3 April 2018

ACCEPTED FOR PUBLICATION
3 May 2018

PUBLISHED
25 May 2018

PAPER

Low-temperature fabrication and characterization of a symmetric hybrid organic–inorganic slab waveguide for evanescent light microscopy

Björn Agnarsson[1,3], **Mokhtar Mapar**[1], **Mattias Sjöberg**[1], **Mohammadreza Alizadehheidari**[2] and **Fredrik Höök**[1,3]

[1] Department of Physics, Division of Biological Physics, Chalmers University of Technology, Fysikgränd 3, SE-412 96 Göteborg, Sweden
[2] Department of Biology and Biological Engineering, Division of Chemical Biology, Chalmers University of Technology, Kemigården 4, SE-412 96 Göteborg, Sweden
[3] Authors to whom any correspondence should be addressed.

E-mail: bjorn.agnarsson@chalmers.se and fredrik.hook@chalmers.se

Keywords: optical waveguides, evanescent-wave microscopy, total internal reflection microscopy, hybrid organic inorganic waveguide, EvSM, biosensing

Supplementary material for this article is available online

Abstract

Organic and inorganic solid materials form the building blocks for most of today's high-technological instruments and devices. However, challenges related to dissimilar material properties have hampered the synthesis of thin-film devices comprised of both organic and inorganic films. We here give a detailed description of a carefully optimized processing protocol used for the construction of a three-layered hybrid organic–inorganic waveguide-chip intended for combined scattering and fluorescence evanescent-wave microscopy in aqueous environments using conventional upright microscopes. An inorganic core layer (SiO_2 or Si_3N_4), embedded symmetrically in an organic cladding layer (CYTOP), aids simple, yet efficient in-coupling of light, and since the organic cladding layer is refractive index matched to water, low stray-light (background) scattering of the propagating light is ensured. Another major advantage is that the inorganic core layer makes the chip compatible with multiple well-established surface functionalization schemes that allows for a broad range of applications, including detection of single lipid vesicles, metallic nanoparticles or cells in complex environments, either label-free—by direct detection of scattered light—or by use of fluorescence excitation and emission. Herein, focus is put on a detailed description of the fabrication of the waveguide-chip, together with a fundamental characterization of its optical properties and performance, particularly in comparison with conventional epi illumination. Quantitative analysis of images obtained from both fluorescence and scattering intensities from surface-immobilized polystyrene nanoparticles in suspensions of different concentrations, revealed enhanced signal-to-noise and signal-to-background ratios for the waveguide illumination compared to the epi-illumination.

Introduction

The extensive progression in the semiconductor and fiber-optic communication industry has led to an escalation in the development of devices based on integrated lightwave manipulation and their deployment outside the main field. In recent years, these optical devices have increasingly been applied in the field of biosensors, mainly because they offer the possibility of realizing a highly compact integrated lab-on-a-chip type of devices but also because they have been shown to offer high sensitivity as well as excellent real-time and label-free detection possibilities [1–4].

Many optical biosensors utilize surface-confined evanescent waves to detect a change in the refractive index close to a surface, induced by some form of surface binding. This change in refractive index is then converted to a readable output signal and correlated to the biomolecular interaction under study [2, 4–12]. Evanescent waves can also be applied in microscopy, such as in total internal reflection (TIR) microscopy, to monitor light scattering induced by surface bound nanoscopic objects label-free [13–16] or to excite fluorescent molecules within the evanescent field [16–19]. Microscopy carried out using evanescent-wave illumination has the important benefit over conventional epi or dark-field microscopy that it provides an illumination profile confined to a very small volume adjacent to the liquid-surface interface, making it possible to follow dynamic processes in highly concentrated environments, such as real biological solutions, without the need for rinsing.

Evanescent wave microscopy can also be realized using planar or slab optical waveguides where the sample (typically in an aqueous solution) forms at least one part of the cladding around an adjacent waveguide core [7, 16, 18–23]. Evanescent wave microscopy carried out using waveguides has some important advantages over conventional TIR microscopy setups. The penetration depth of the evanescent field in conventional TIR microscopy is usually limited to around 200 nm from the surface whereas for waveguides this depth can in principle be tuned to a value of choice by carefully selecting and controlling the waveguide geometries and optical properties [24]. Waveguides can furthermore generate a more even illumination field compared to that typically achievable with TIR illumination and can be extended over macroscopic areas. Further, objective based TIR microscopy requires specialized and expensive high numerical aperture objectives, while with waveguide illumination the paths of the excitation and detection light are independent and thus puts no restrictions on the objectives used for light collection.

Conventionally, optical waveguides are either all-inorganic (insulators or semiconducting materials) or all-organic (polymers, conductive polymers and/or biologically produced substances). Organic materials offer a wider range of physical properties compared to their inorganic counterparts, allowing properties such as refractive indices, thermal and elastic coefficients to be better matched to desired specifications [25]. Polymers can furthermore be directly spin-coated on surfaces, making the need for highly sophisticated deposition machinery unnecessary. On the other hand, inorganic materials offer higher structural and compositional purity and also tend to be more structurally robust and chemically inert than organic materials. It is also easier to chemically modify their surface properties, which offers an advantage in bioanalytical contexts. Multilayer structures composed of both inorganic and organic layers could in principle combine the best of both worlds, but they are generally difficult to realize, mainly because of large differences in thermal expansion coefficients that results in layer delamination and/or crack formation. In this work, we present a low-temperature fabrication method (schematically illustrated in figure 1) to obtain a three-layered symmetric hybrid organic–inorganic slab waveguide-chip intended for carrying out evanescent-wave microscopy in aqueous environments. In brief, the chip are made by forming inorganic films (either SiO_2 or Si_3N_4) within an organic cladding layer (CYTOP^{TM}), with a refractive index ($n = 1.34$) close to that of water. The waveguide-chip was furthermore designed to support only the fundamental optical mode, which ensured efficient but-coupling (schematically illustrated in figure 2) and highly confined and well-characterized light propagation. The chemically inert inorganic core layer ensured that standard surface modifications could be directly applied to the surface, a property that in this context has already been utilized for studying biologically relevant processes [16, 26]. Further, the organic cladding layers provided the structure with a much-desired matching of refractive index to that of water, which thus formed an 'invisible' part of the cladding environment. This, in turn, ensured low background light scattering, which enabled direct detection of scattered evanescent light from nanoscopic objects on the core layer. We furthermore tested the performance of the waveguide by characterizing some of its fundamental optical properties. The thickness and refractive index of all layers were measured using spectroscopic ellipsometry and from that, a visual profile of the guided light in the waveguide could be constructed and compared to a measured profile obtained by imaging the end-facet of the waveguide. The measured profile was then used to evaluate the penetration depth of the chip with respect to both theory and simulation. The propagation loss due to scattering and dielectric absorption was evaluated and discussed in relation to other waveguide devices used in similar contexts. Finally, the performance of the waveguide was compared to conventional epi-illumination microscopy by quantitative analysis of the measured scattering and fluorescence intensities from 100 nm in diameter surface-adsorbed polystyrene beads in suspensions of different concentrations.

Chip fabrication

Due to the large difference in thermal expansion coefficients between the organic CYTOP layers and the inorganic core layer, mechanical stress is likely to develop during the core layer deposition. This stress can be reduced by forming the core layer in multiple steps and by allowing it to relax over time in atmospheric pressure between depositions. Slow deposition performed using low processing powers may help, both in order to keep the processing temperature low and to minimize stress build up between the layers, but it may also influence the

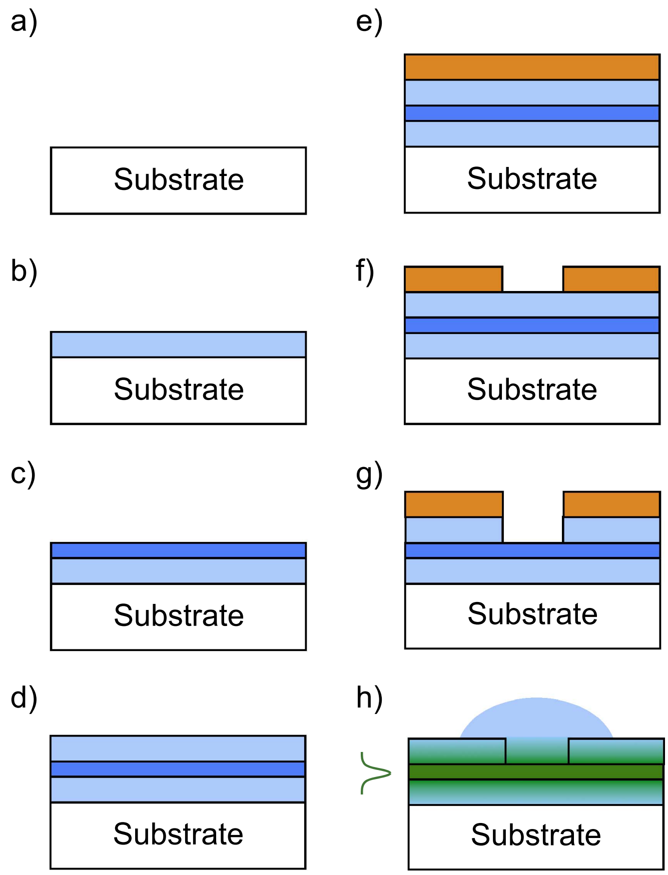

Figure 1. Process flow for the fabrication of the waveguide-chip (structures not to scale). (a) Substrate pretreatment; (b) CYTOP bottom cladding layer coating and Al deposition; (c) Al removal and coating/deposition of waveguide core layer; (d) coating with CYTOP top cladding; (e) coating of photoresist and patterning of sensing region by UV exposure; (f) development of exposed pattern; (g) reactive-ion etching and forming of sensing regions; (h) photoresist layer removal, fiber light in-coupling and introduction of the aqueous sample to the sensing region.

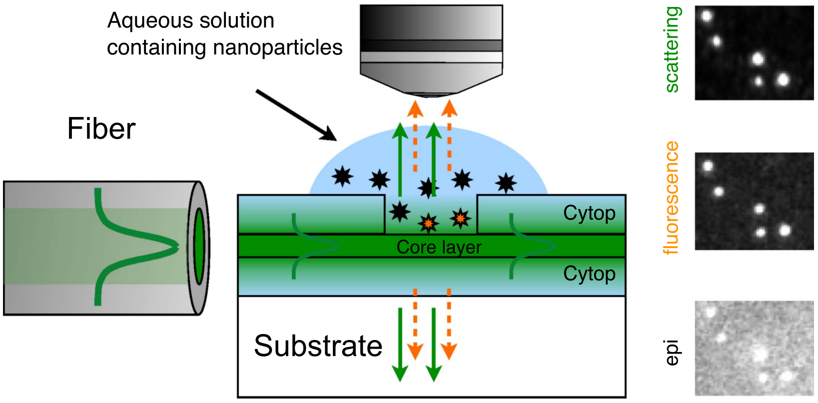

Figure 2. Schematic representation of the waveguide-chip. A single mode optical fiber is aligned to the facet of the waveguide and light (green) is coupled into the core layer. An opening is constructed in the upper cladding layer into which a solution containing the specimen of interest is placed. The evanescent light at the interface between the core and the upper cladding will interact with objects within its penetration depth either through absorption and fluorescence (orange dashed arrows) or scattering (solid green arrows). The generated light is then collected using a standard objective of choice in an upright or inverted configuration or in a combination of both. The insets to the right show the effect that the evanescent illumination has on the signal contrast from surface-adsorbed 100 nm in diameter fluorescent particles compared to conventional epi-illumination (the insets are adopted from figure 5 in the succeeding section). The insets are approximately 6 μm wide.

optical and structural quality of the core layer, for good or for bad. To avoid crack-formations, it is necessary to keep all processing temperatures below the glass-transition temperature of the CYTOP polymer, which is approximately 110 °C. Another key aspect is to ensure adequate adhesion between the different layers of the inorganic-organic structure. In some cases, this can be difficult to achieve, but with the use of appropriate adhesion promoters or specially designed surface treatments, sufficiently strong adhesion can be realized.

The choice of core layer material is important for two reasons: first because of its optical properties such as refractive index, surface flatness and light attenuation, which influence both the modal profile (penetration depth) of the guided light and the amount of stray-light (background) scattering and secondly because of its chemical properties, which are of key importance when it comes to functionalizing the surface.

For optimal performance, the waveguide fabrication processing should be carried out in a standard class-1000 (Fed. Std. 209 E) cleanroom on an optically flat supporting surface, such as a polished silicon wafer or an transparent glass wafer. The individual processing steps employed for the waveguide structure characterized in this work are essentially the same as those previously used for fabrication of a similar symmetric polymer waveguide structure [27] (see figure 1) and can be roughly divided into three parts: the lower cladding layer; the core layer and the upper cladding layer.

A homogenous optically flat supporting surface helps minimizing losses in the waveguide since any surface irregularities, contamination or debris are likely to cause structural defects in the final structure, which can affect the performance (attenuation and stray-light scattering) of the waveguide. Depending on the quality (smoothness, cleanliness, prior handling etc.) of the supporting substrate used, some form of substrate cleaning, such as plasma ashing, may be necessary to help rid the surface of contamination. Furthermore, baking the support to temperatures >200 °C for a few minutes removes water from the surface (dehydration bake), which may help to improve adhesion between the support and the waveguide structure. However, in our case where the waveguide was fabricated on a silicon wafer, such steps were found to be unnecessary. Before applying the first layer of CYTOP, the supporting surface had to be primed to ensure adequate adhesion. For silicon and glass supporting substrates, we found that a silane adhesion layer made from a mixture of APTES ($H_2N(CH_2)_3Si(OC_2H_5)_3$ (3-Aminopropyl)triethoxysilane), from Sigma-Aldrich, with filtered deionized water and ethanol, in the volume ratios 1:25:475 respectively, resulted in a satisfactory adhesion between substrate and CYTOP. A freshly prepared mixture was applied directly to the surface and spin-coated at 4000 rpm for 30 s before being heated on a hotplate at approximately 60 °C for 2 min to remove all traces of solvents from the surface (figure 1(a)).

After priming, CYTOP CTX-809AP2 was spin-coated on the wafer at 1000 rpm for 1 min. Solvent removal and annealing was carried out by placing the wafer in a convection oven under a glass cover in atmospheric ambient. The role of the cover glass was to ensure high surface flatness and to avoid particle contamination during the extended baking process [27]. The oven temperature was kept at 50 °C for 60 min to remove traces of gas and bubbles in the resin. The temperature was then ramped to 80 °C over 15 min and maintained at 80 °C for 1 h to remove solvents from the layer. Thereafter the temperature was again ramped to 250 °C over 80 min and maintained for 3 h. After natural cool-down, this baking process resulted in an approximately 4 μm thick layer of CYTOP (figure 1(b)) with root mean squared surface roughness of about 0.5 nm (see the supporting information, available online at stacks.iop.org/NANOF/2/025007/mmedia). In principle, there is no upper limit for the lower cladding layer thickness, but it must be thick enough to prevent interaction between the guided mode and the underlying substrate.

CYTOP is naturally hydrophobic which makes subsequent film-coating challenging. To overcome this problem a thin aluminum layer (or a layer of another suitable metal) can be deposited on the hardened CYTOP layer and subsequently removed by wet etching [28–30]. A thin layer (20 nm) of aluminum was deposited on the CYTOP surface using e-beam evaporation and subsequently removed by placing the wafer in a solution of sodium hydroxide (or ma-D331, photoresist developer from Micro Resist Technology GmbH) for 2 min, and thereafter in deionized water for approximately 1 min before being blow-dried using filtered nitrogen. This treatment increased the wettability of the CYTOP layer and ensured adequate adhesion to the subsequently applied core layer.

The core layer can in principle be made of any optically transparent material with refractive index higher than that of the surrounding cladding layers. However, this step should not involve any heating to temperatures surpassing the glass-transition temperature of the cladding layers since that might result in crack-formations or delamination of the core layer from the cladding layer. The core layer can be made with chemical or physical vapor deposition, thermal evaporation (resistive or e-beam) or any other standard cleanroom deposition method. For waveguides with a spin-on-glass (SOG) core layer, the layer was formed by spin-coating SOG (IC1-200 from Futurrex Inc.) on top of the lower cladding layer at spin-speeds corresponding to the desired thickness and hardened in a vacuum conduction oven at 120 °C for 24 h (figure 1(c)). The vacuum-oven baking ensures fast solvent evaporation and results in a flat surface (see the supporting information), which is desirable to obtain low stray-light (background) scattering and low attenuation. The thickness of the core layer should be chosen carefully since it is one of the factors that influences the modal profile of the guided light and thus the penetration depth of the evanescent field into the sample (see discussion in the following section).

The upper cladding of the waveguide was formed by spin-coating a second layer of CYTOP on top of the core layer (figure 1(d)), using the same spin-coating settings as used for the lower CYTOP layer. The wafer was then placed in the vacuum-oven at 50 °C for 30 min to eliminate gas and bubbles from the resin, after which the temperature was increased to 80 °C at a ramping speed of 2 °C min^{-1} and left for 30 min before ramping the temperature to 100 °C at 2 °C min^{-1}. The wafer was then baked for one hour before being cooled to room temperature inside the oven. The surface flatness of this layer is not as critical as for the first CYTOP layer, and hence, the use of cover glass could be skipped during this baking step.

A sensing region was then formed in the upper cladding layer in which the core layer can be exposed to the aqueous solution containing the sample to be measured. This region can be of any size and shape and can be made using a hard-mask (metal) or some form of resist (e.g. photoresist, e-beam resist). In our case a mask was made using positive photoresist (ma-P 1225, Micro Resist Technology GmbH), which was spin-coated on the aluminum pre-treated (aluminum deposited and removed as described for the first CYTOP layer) CYTOP layer at 2000 rpm for 30 s and subsequently baked at 100 °C for 5 min on a standard hotplate (figure 1(e)). The photoresist was then exposed to ultraviolet light through a mask and developed for 2 min in ma-D331 developer before being rinsed in deionized water and blow-dried using nitrogen. This left the upper CYTOP layer partially exposed as indicated in figure 1(f). Reactive-ion etching (RIE) was then applied to etch through the exposed CYTOP layer (~4 μm) to form the sensing region (figure 1(g)). Since etching rates vary between different etching systems, a thorough etching calibration needs to be carried out to obtain the exact etching rates for the cladding- and resist layers. In our case etching was carried out in three steps: first for 2 min in pure O_2 (40 sccm), then for 8 min in an O_2/Ar (40:40 sccm) mixture and finally for 2 min in pure O_2 (40 sccm). Argon is chemically inert but its plasma helps to mechanically sputter undesired inorganic fragments that can be found within the sensing region of the chip. Argon also increases the anisotropy of the etching, making it more directional [31]. The oxygen on the other hand chemically etches the CYTOP but will leave inorganic core layer more or less unaffected as the etching reaches through the CYTOP. To achieve a highly anisotropic etching, chamber pressure was kept relatively low. In our case the etching power was set to 100 W and chamber pressure was kept at 30 mTorr. After RIE, the exposed core layer is highly reactive, so in order to neutralize it, the wafer was placed in deionized water for a few minutes, before being blow-dried using filtered nitrogen.

Wafer dicing can be carried out using standard wafer dicing machinery. Prior to dicing, a layer of photoresist or other suitable material should be spin-coated on the wafer to protect the sensing regions from debris and other contaminating elements. To ensure highly efficient end-fire coupling of light into the waveguide, the facets of the chips need to be as smooth as possible. This requires the dicing parameters, such as blade type, blade rotation speed and feed rate, to be optimized for each fabrication facility. Following dicing, the protective layer and mask layer was removed by soaking the chips in alkaline photoresist remover (ma-R 404, Micro resist technology GmbH) for 10 min, and thereafter in deionized water for approximately 5 min before being blow drying using nitrogen. The chips can then be stored in a closed container in a cupboard until use (figure 1(h)).

Optical properties and characterization

A simple micrometer translational stage is used to carefully align a single mode optical fiber to the facet of the waveguide-chip (figure 2). Once properly aligned, light can be easily coupled into the chip. An aqueous solution containing the specimen of interest is then placed in the sensing region of the chip. Since the refractive index of the cladding layer is closely matched to that of the solution, stray-light (background) scattering generated at the interface between the organic cladding layer and the sensing region is minimized. Using this configuration, the scattering of evanescent light by nanoscopic objects on the surface, such as dielectric (viruses, lipid vesicles, polystyrene beads, etc.) or metallic nanoparticles, can be directly detected (green arrows in figure 2). The evanescent light can also be used in a more conventional way, to generate fluorescence from labeled objects as in TIR fluorescence microscopy [17] (orange dashed arrows in figure 2).

Hybrid waveguide-chips with SiO_2 and Si_3N_4 core layers were fabricated using four different fabrication techniques: spin-coating plasma enhanced chemical vapor deposition, physical vapor deposition (direct-current sputter deposition) and electron-beam evaporation. Besides from having different chemical and morphological properties, these different core layers express different optical characteristics, which affect the stray-light scattering and penetration depth of the evanescent field. The core layer material dispersion depends not only on the specific type of material, but also on the different processing techniques used (see figure 3(a)). Although not shown here, the dispersion and surface morphology are also highly influenced by the specific processing parameters used, such as chamber pressure, processing powers and temperature, and hence, results may vary between different processing facilities. Using the measured refractive indices of the core and cladding layers, the penetration depth ($d(t)_p$) of the evanescent light into the cladding/water can be calculated as a function of core

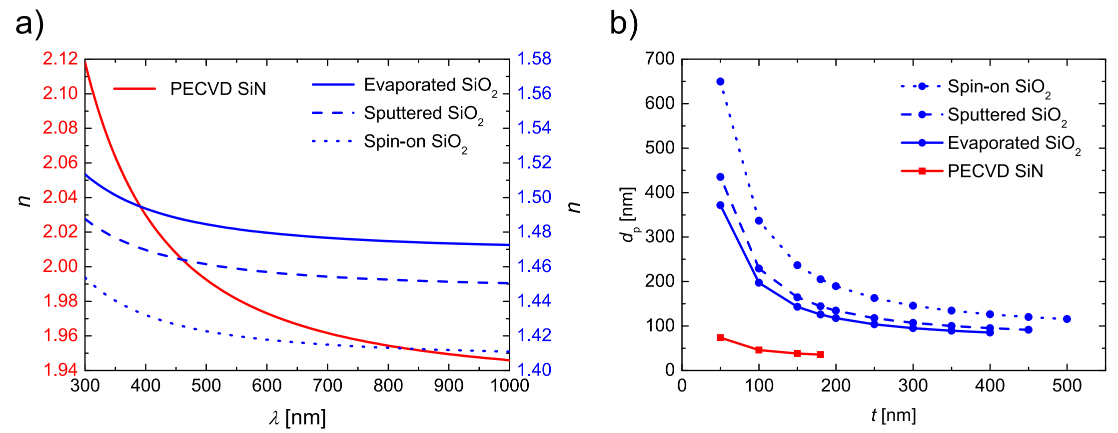

Figure 3. (a) Dispersion curves, measured using a spectroscopic ellipsometry, for different core layers on CYTOP. The left scale bar applies to the Si_3N_4 layer (red) while the right scale bar applies to the SiO_2 layers (blue). Both scale bars have the same span. (b) Calculated (according to equation (1)) penetration depths for a 532 nm TE polarized light into the CYTOP cladding for the different core layers measured in (a). Only results for core layer thicknesses where single mode behavior is observed are shown.

layer thickness (t) using the following equation [24]:

$$d(t)_{\mathrm{p}} = \frac{\lambda}{4\pi} \frac{1}{\sqrt{n(t)_{\mathrm{eff}}^{\ 2} - n_{\mathrm{w}}^{\ 2}}}, \tag{1}$$

where λ is the vacuum wavelenght of light (532 nm, TE polarized laser), n_{w} is the refractive index of water at 532 nm and $n(t)_{\mathrm{eff}}$ is the effective refractive index experienced by the fundamental TE mode of the guided light in the waveguide structure. Using a one-dimensional mode solver, $n(t)_{\mathrm{eff}}$ can be attained numerically [32]. For Si_3N_4, a single mode propagation will be observed for a core layer thicknesses up to around 180 nm, while SiO_2 core layers will exhibit single mode behavior up to thicknesses around 400–500 nm, depending on the particular deposition method used (see figure 3(b)). Under the reasonable assumption that equation (1) is applicable for the investigated chip design, waveguides composed of Si_3N_4 core layers should have penetrations depths well below 100 nm, while the SiO_2 waveguides have penetration depths ranging between 100 and 700 nm. The material of choice for SiO_2 core layer waveguides is SOG; mainly because it yields a smooth and flat surface and thus minimizes light attenuation and stray-light scattering and, because from a manufacturing point of view, it makes the fabrication more economical and simple compared to when more sophisticated cleanroom deposition techniques are used (see atomic-force microscopy images in the supporting information).

For optical characterization and testing, a SOG waveguide-chip (500 nm thick core layer) was placed under an upright Olympus X61 microscope, equipped with: a 100 W mercury light source for epi illumination, high contrast filter cubes (FITC/TRITC/BF), an Olympus 2X, NA 0.08 objective and a Zeiss 100X, NA $=$ 1.0 water immersive objective. A Hamamatsu ORCA-Flash4.0 CMOS camera was used for image acquisition. The intensity of all images presented here have been normalized by linearly mapping 99.5% of the intensity histogram of the raw image data onto a 256-level gray scale with the zero-level unchanged. The images have not, in any other way, been adjusted or tempted with. A 532 nm fiber-coupled NANO 250 (Qioptiq, Inc.) laser module was used as a single mode light source.

When TE polarized, 532 nm light is coupled into the waveguide-chip, the throughput signal at the end-facet of the chip exhibits a highly confined mode with a uniform in-plane intensity distribution (see micrograph in figure 4(a)). Finite-element simulations of the light propagation for an identical waveguide structure reveal a well-defined single mode profile (figure 4(a), red dotted curve). After adding the effect of diffraction-limited resolution of the imaging optics used (see the supporting information) to the simulated profile (figure 4(a), red solid curve), an excellent agreement is obtained between the simulated and the experimentally determined mode-widths (figure 4(a), black circles). Taking into account the 500 nm thickness of the SOG core layer (blue shaded area in figure 4(a)), the effective penetration depth of the evanescent light converts to around 110 nm, which is in excellent agreement with the expected value obtained with the one-dimensional mode solver for the structure (figure 3(b), blue dotted curve).

An estimation of the light attenuation through the chip can be obtained by collecting the light scattering from surface-adsorbed objects or contaminants as a function of distance as the light propagates through the chip. This method measures both the propagation loss due to scattering and dielectric absorption in the waveguide. To ensure detectable scattering from the surface, a suspension containing low concentration of 50 nm gold particles was introduced to the sensing region of a SOG chip, allowing the particles to adhere to the surface. After subsequent rinsing, the scattering signal from the sensing region of the surface was collected using

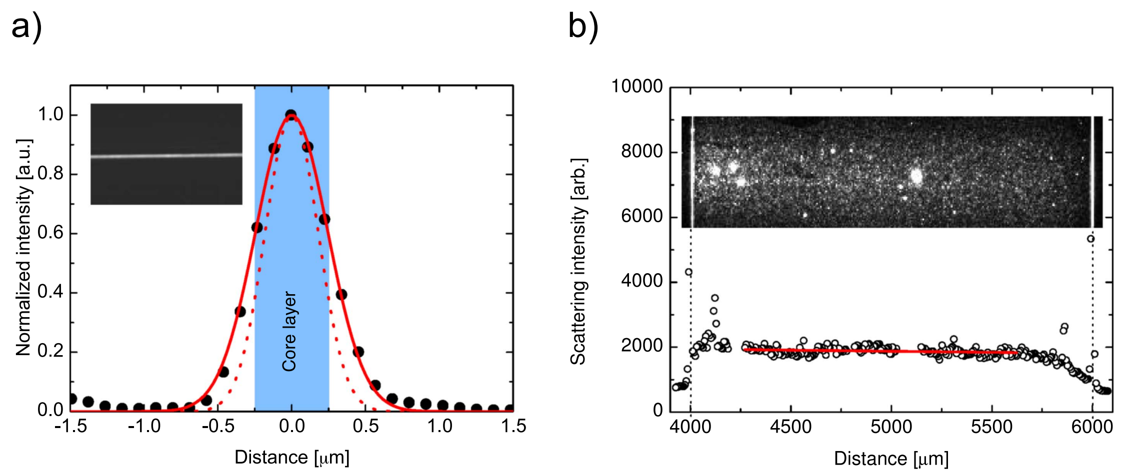

Figure 4. Optical characteristics of a hybrid SOG waveguide-chip with 500 nm thick SOG core layer. (a) A micrograph showing a highly confined single mode output obtained at the far side of the waveguide-chip. The filled circles represent the normalized measured intensity profile over the output while the red curves represent the theoretical values before (red dotted line) and after (red solid line) accounting for the finite resolution of the imaging optics (see the supporting information). The shaded blue area represents the core layer of the waveguide. (b) A micrograph showing the surface scattering from surface-adsorbed 50 nm gold particles in aqueous environment. The edges of the sensing region are visible as white, high intensity lines 2 mm apart on each side. The graph shows the scattered intensity profile across the chip's sensing area with the red solid line representing an exponential fit to the data.

a 2 × objective and the intensity profile fitted to an exponentially decaying function, revealing a loss of about 1.5 dB cm^{-1} (figure 4(b)), which is comparable to reported loss values for waveguide devices of similar kind [18, 33, 34].

Waveguide performance

To evaluate the waveguide's performance, signal-to-background ratios (SBRs) and signal-to-noise ratios (SNRs) from discrete surface-adsorbed fluorescent polystyrene beads were evaluated and directly compared on an individual particle level, with SBRs and SNRs obtained using standard epi illumination. To mimic kinetic measurements in real complex biological solutions, image acquisition was carried out in suspensions containing various concentrations of polystyrene beads in bulk. A comparison was also made between the SNRs and SBRs from the scattered and fluorescent signals for three input intensities for the evanescent light.

A suspension containing the fluorescent beads with a nominal diameter of 100 nm (Phosphorex, Inc.) was introduced to the sensing region of the chip, which had been functionalized with a mixture of poly(L-lysine)-g-poly(ethylene glycol) (PLL(20)-g[3.5]-PEG(5), SuSoS AG, Switzerland) and PLL(20) in ratio (1000:1). The PEG chains prevent adsorption of the negatively charged beads while the positively charged PLL electrostatically attract and adsorb the beads to the surface. Images where then acquired subsequently using waveguide and epi-illuminations for solutions containing different concentrations of beads in bulk and for different illumination intensities. All images were acquired in succession using identical camera settings (50 ms exposure, and 2 × 2 binning) and same objective (100×, 1.0 NA, WD = 1 mm). The suspensions were prepared by diluting the polystyrene stock solution (10 mg ml^{-1} or 2.5×10^{12} beads ml^{-1}) in deionized and filtered water (MQ) in ratios 1:100 (*High concentration*, 100 µg ml^{-1} or 2.5×10^{10} beads ml^{-1}), 1:1000 (*Medium concentration*, 10 µg ml^{-1} or 2.5×10^{9} beads ml^{-1}) and 1:10 000 (*Low concentration*, 1 µg ml^{-1} or 2.5×10^{8} beads ml^{-1}). For the epi illumination, a 100 W mercury arc lamp operated at maximum light intensity was used while the waveguide illumination was carried out at different intensities using the same single mode, 532 nm, TE polarized fiber-coupled light source as before.

When images of adsorbed fluorescent beads are obtained through a suspension containing beads, the contrast difference between the different illumination schemes becomes clear, with both the scattered evanescent signal (WGS) and the evanescently excited fluorescent signal (WGF) showing higher contrast compared to the epi-illumination excited fluorescent signal (epi, figure 5). The observed difference in contrast between the three images depends, in this particular case, on several factors. First, the out-of-focus fluorescence from beads in solution will contribute to an increased background intensity in the image obtained using the epi-illumination (seen as brighter/higher background in the epi image in figure 5). The effect of out-of-focus fluorescence of beads in solution is, however, not observed in the images obtained using the waveguide illumination (seen as darker background in the WGF and WGS images) due to the short penetration depth of the

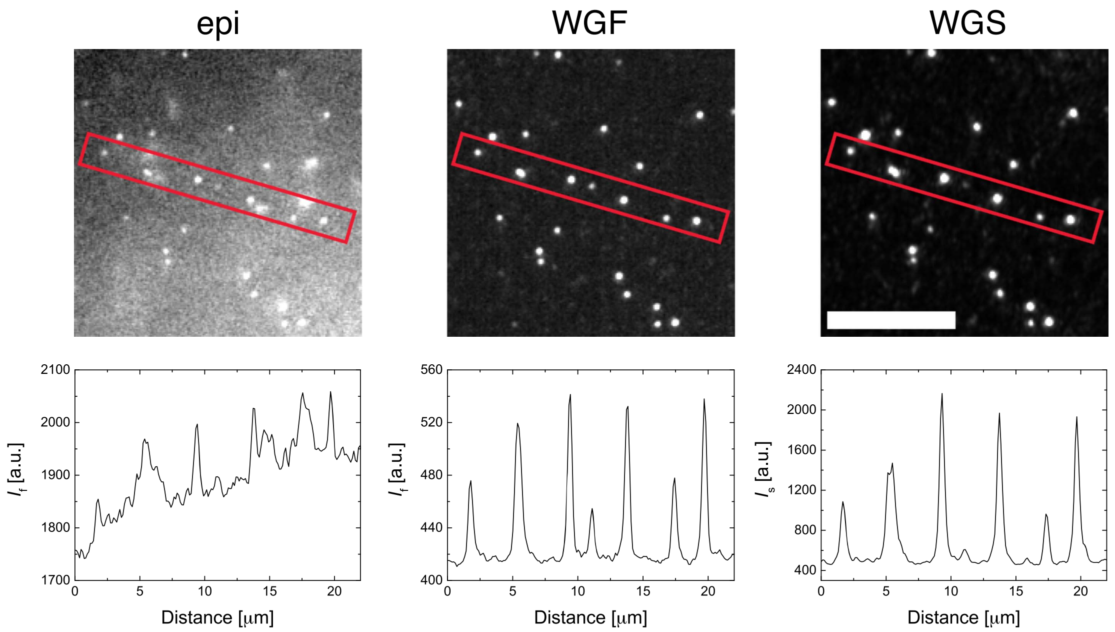

Figure 5. Images of 100 nm in diameter fluorescent beads in 2.5×10^9 beads ml^{-1} suspension (*Medium concentration*) obtained using epi-illumination and fluorescence signal detection (epi), waveguide illumination and fluorescence (WGF) and scattering (WGS) signal detection and their corresponding intensity profiles. Here the illumination intensity for the waveguide illumination is set to *Max intensity* (see text for definition). Scale bar represents 10 μm.

evanescent light ($d_p \sim 110$ nm). Also, as both scattering and fluorescence signals must pass through the suspension before reaching the objective (1 mm working distance), the concentration of polystyrene beads in bulk will influence the level of observed contrast, since both scattered and fluorescent light will interact with beads in suspension. This, however, is a consequence of the particular experimental setup and is independent of the specific illumination method used and can be circumvented e.g. by placing a glass coverslip over the sensing area [20] or by employing an inverted microscopy setup and viewing the adsorbed beads from beneath. Generally, the WGS signal will have a greater dependence on size, shape and vertical position of the measured object compared to both the WGF and epi signals, which can either be an advantage or a disadvantage, depending on the particular experimental study.

To compare the contrast difference between the three different detection methods, the SNR and SBR were calculated for individual beads according to:

$$\mathrm{SNR} = \frac{I_s - I_B}{\sigma_b}, \tag{2}$$

$$\mathrm{SBR} = \frac{I_s - I_B}{I_B}, \tag{3}$$

where I_s represents the integrated signal intensity from a single bead, I_B is its average local background ($I_B = \sum_{\text{Bead area}} I_b$) and σ_b is the standard deviation of the local background (see the supporting information). The SNR and SBR from 1650 individual adsorbed beads were measured for the different illumination schemes in different suspensions and compared on the basis of individual beads.

In figure 6 the SNR and SBR from the surface-adsorbed beads are compared between different laser intensities and different suspensions containing different bead concentrations. Here, *Max intensity* corresponds to the maximum intensity exciting the optical fiber, while *Medium* and *Low intensity* correspond to approximately 25% and 2% of that value (see the supporting information).

The SNR for WGS shows only a moderate increase with increasing input intensity (figure 6(a)) while for the WGF the dependence on input intensity is greater (figure 6(c)). The difference can be explained by the relatively large and small increase in the standard deviation of the background (σ_b) for the WGS and WGF signals, respectively, with increasing input intensity. For both WGS and WGF the SNRs are more or less independent of bead concentration in bulk, with the SNR in WGF showing only a moderate decreasing trend by a factor of ~4, that can be attributed to photobleaching. The SNR of the epi signals does, however, show a large dependence on the concentration of beads in bulk, with median SNR decreasing by factor ~30 between measurements conducted in highly concentrated conditions and in MQ (figure 6(e)), clearly illustrating the large effect of out-of-focus fluorescence on the measured signal for epi-illumination.

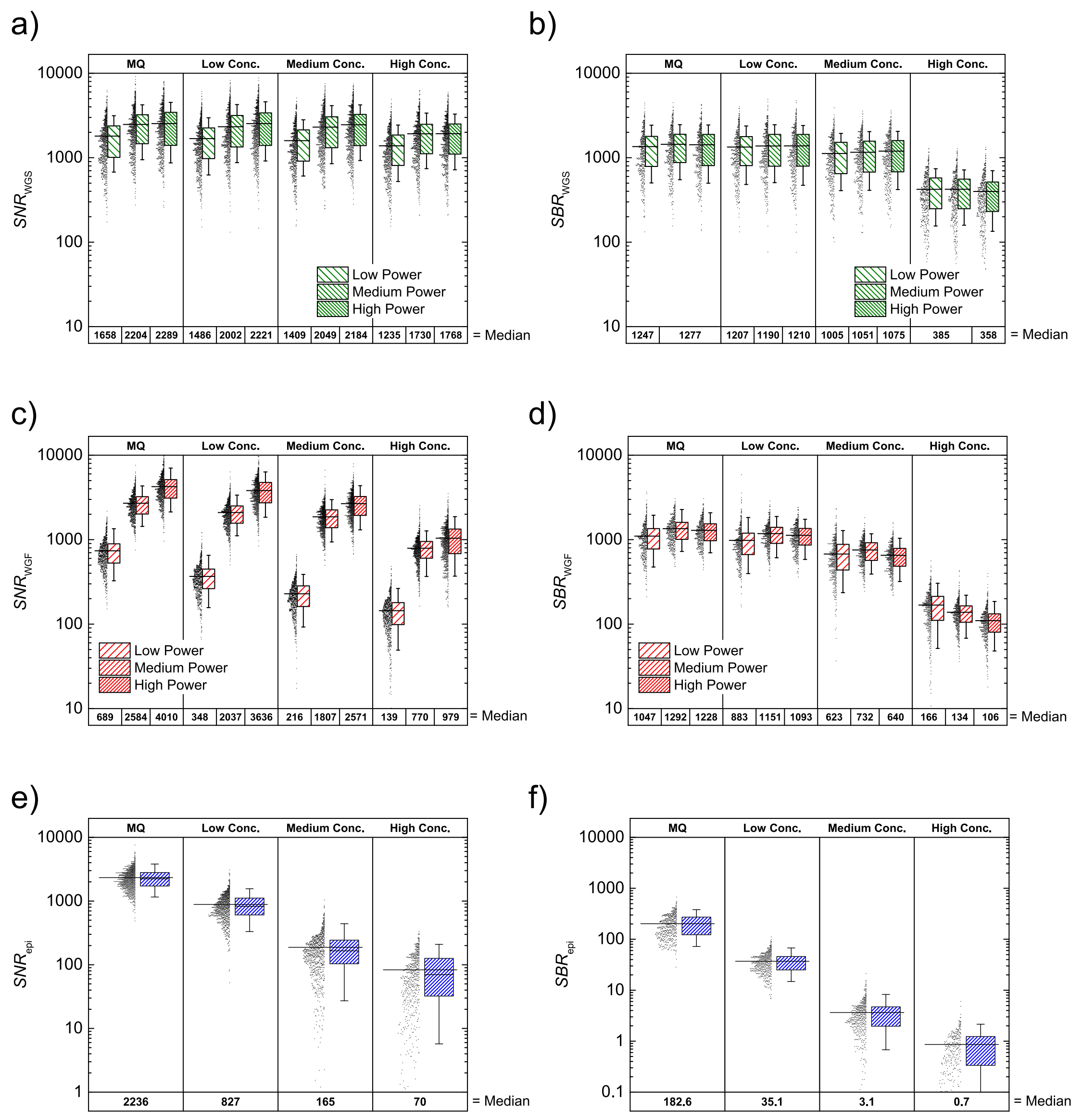

Figure 6. SNR and SBR for waveguide and epi-illuminations of fluorescently labeled polystyrene beads (100 nm in diameter), in suspensions containing different bead concentrations (MQ $= 0\ \mu\text{g ml}^{-1}$, *Low concentration* $= 1\ \mu\text{g ml}^{-1}$ or 2.5×10^{8} beads ml^{-1}, *Medium concentration* $= 10\ \mu\text{g ml}^{-1}$ or 2.5×10^{9} beads ml^{-1} and *High concentration* $= 100\ \mu\text{g ml}^{-1}$ or 2.5×10^{10} beads ml^{-1}), measured using different illumination intensities. (a) and (b) Are constructed from waveguide scattering signals (WGS). (c) and (d) Are constructed from the waveguide fluorescent signal (WGF) and (e) and (f) are constructed from epi-fluorescence data. The whiskers represent the 10%–90% range of the data set, the box 25%–75% range and the horizontal line in the middle of the box represents the mean value. The *x*-axis shows the median of the data.

When the SBR values were instead compared, the behavior was somewhat different. Both the WGS and WGF signals showed SBR to be independent of input intensity, but a slight decrease was observed when the signals were measured in solutions containing high concentrations of beads (figures 6(b) and (d)). This behavior can be explained with reference to equation (3). For both the WGS and WGF data, the signal (I_s) and background (I_B) intensities were proportional to the input intensity in the same way, meaning that the net effect of increasing the input intensity canceled out. In highly concentrated solutions the decrease was simply the result of a higher background due to increased number of beads found within the penetration depth of the excitation field. The effect of photobleaching was again somewhat visible in the WGF data. For the epi data, the effect of bulk concentrations on SBR was even greater than for the SNR, with median SBR decreasing by a factor of almost 300 in highly concentrated solution compared to MQ (figure 6(f)). However, in the highly concentrated solution, only around 0.5% of the surface-adsorbed beads could be detected in epi (see supporting information), with the rest being either invisible or having a SBR below 1.

To make the comparison between epi and waveguide illumination as accurate and objective as possible, the excitation rates of the fluorophores has to be close to identical for the two illumination schemes [35]. To achieve

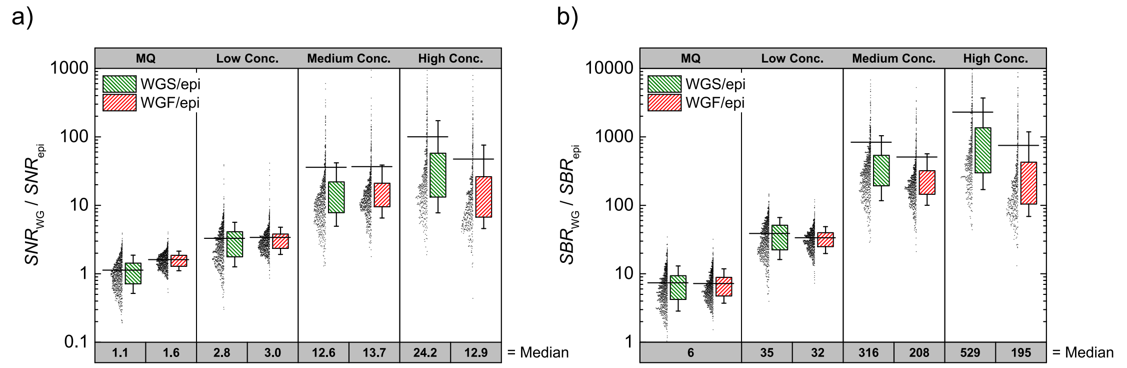

Figure 7. Direct comparison between epi and waveguide illumination schemes for the data shown in figure 6. (a) SNR ratio and (b) SBR ratio between waveguide illumination (set to 45% of *Max intensity*) and epi-illumination obtained by comparing over 1650 individual surface-adsorbed beads in suspensions containing four different bead concentrations. The whiskers represent the 10%–90% range of the data set, the box 25%–75% range and the horizontal line represents the mean value. The *x*-axis shows the median of the data.

this, the rate of photobleaching for the waveguide illumination was measured for various input intensities and compared to the corresponding bleaching rate for epi illumination. In our case, the same amount of photobleaching was achieved with an input intensity corresponding to 45% of the maximum excitation intensity (*Max intensity*) (see the supporting information). When measured in MQ, the advantage of evanescent illumination over epi was only minimal while in highly concentrated suspensions the difference in SNR and SBR could be quite large, an 12.5 and 192-fold increase in the median WGF signal and 23.7 and 527-fold in the median WGS signal, respectively (see figures 7(a) and (b)). In suspensions containing *Low* and *Medium* bead concentrations, the advantage of WGF and WGS over epi illumination was close to equivalent, but in highly concentrated solutions the WGS signal gave slightly higher values, which might partly be due to photobleaching. Since the fluorescence signal from a bead scales with its volume while the scattering scales with its volume squared, inhomogeneity in bead sizes will lead to a wider distribution in the scattering than in fluorescence intensity. Another factor that influenced the spread in data was the illumination profile of the light. For waveguide illumination, the profile was quite uniform over the field of view while the epi-illumination had a rather uneven illumination profile due to shading effect (see the supporting information) [36], which lead to an increased spread in epi data [36].

Conclusions

Herein, we have described in detail the fabrication process and characteristics of a novel hybrid organic–inorganic waveguide-chip for use in evanescent-wave microscopy. The use of SOG as a core layer allowed for simple and inexpensive fabrication processing while retaining compatibility with standard glass surface chemistries. The chip has in previously published studies proven its worth with various surface modification schemes [16] and has been successfully implemented for studying nanoscopic objects, from single gold nanoparticles [37, 38] and vesicles [26] to cells [16]. In this work, we furthermore tested the chip's performance and demonstrated how the ratios of $\mathrm{SNR}_{\mathrm{WG}}/\mathrm{SNR}_{\mathrm{epi}}$ and $\mathrm{SBR}_{\mathrm{WG}}/SBR_{\mathrm{epi}}$ increase with increasing suspension concentration (see figures 7(a) and (b)), confirming the advantage of evanescent illumination over standard epi-illumination schemes for measurements in concentrated solutions. Other similar evanescent illumination techniques, utilizing either waveguides [22, 39] or dark-field [13, 14, 40, 41] microscopy setups, have shown similar enhancements in SNR and SBR compared to epi-illumination, but direct comparison between different devices and illumination arrangements is rather difficult to make since the absolute values will depend on the particular experimental setups.

The SBR ratios obtained using the waveguide were substantially better than that of the epi-illumination, even when low excitation intensities were used. At *Low intensity* (excitation intensity experienced by beads corresponding to roughly 4% of the epi illumination intensity), the differences in SBRs were ~230 and ~550 fold for the WGF and WGS, respectively, when measured in a highly concentrated suspension (see figures 6(b), (d) and (f)). Lowering the excitation intensity had the clear advantage of reducing photobleaching and other possible undesired photochemical effects, which can be beneficial for example in extended time-lapse imaging, but it also reduces the measured signal intensity. The negative effect of photobleaching can be seen in the WGF data (figure 6(d)), with SBR slightly dropping with increasing excitation intensity, while obviously, such an effect was not observed in the WGS data (figure 6(b)), signifying a great advantage of relying on scattered rather than fluorescent signals in measurements like these.

In general, both the scattering and fluorescence signals reveal images with excellent contrast, making the chip highly suitable for applications that require either ultra-sensitive fluorescence imaging, such as single-molecule detection, or label-free detection of nanoparticles on surfaces, with high spatial and temporal resolution. High SBR is also important for designing photon-limited experiments [42].

The chip can be used in various applications where highly confined illumination at surfaces is required and allows for evanescent-wave illumination to be carried out with a wide range of possible penetration depths and wavelengths over macroscopic areas. The open design of the chip makes integration of both microfluidic components and other complementary modalities, such as atomic-force microscopy simple and effortless. It can easily be used as an add-on to any conventional upright or inverted microscope and, except from a single mode light source, requires no additional apparatus or any special requirements being placed on either the objectives or the camera used for image acquisition.

Acknowledgments

This work is funded by the Swedish Research Council and the EMRP project HLT04 'BioSurf'. The EMRP is jointly funded by the EMRP participating countries within EURAMET and the European Union.

ORCID iDs

Björn Agnarsson https://orcid.org/0000-0003-3364-7196

References

[1] Velasco-Garcia M N 2009 Optical biosensors for probing at the cellular level: a review of recent progress and future prospects *Semin. Cell Dev. Biol.* **20** 27–33

[2] Estevez M C, Alvarez M and Lechuga L M 2012 Integrated optical devices for lab-on-a-chip biosensing applications *Laser Photonics Rev.* **6** 463–87

[3] Kozma P, Kehl F, Ehrentreich-Forster E, Stamm C and Bier F F 2014 Integrated planar optical waveguide interferometer biosensors: a comparative review *Biosens. Bioelectron.* **58** 287–307

[4] Fernandez Gavela A, Grajales Garcia D, Ramirez J C and Lechuga L M 2016 Last advances in silicon-based optical biosensors *Sensors* **16** 285

[5] Taitt C R, Anderson G P and Ligler F S 2005 Evanescent wave fluorescence biosensors *Biosens. Bioelectron.* **20** 2470–87

[6] Vörös J *et al* 2002 Optical grating coupler biosensors *Biomaterials* **23** 2699–3710

[7] Grandin H M, Städler B, Textor M and Vörös J 2006 Waveguide excitation fluorescence microscopy: a new tool for sensing and imaging the biointerface *Biosens. Bioelectron.* **21** 1476–82

[8] Leung A, Shankar P M and Mutharasan R 2007 A review of fiber-optic biosensors *Sensors Actuators* B **125** 688–703

[9] Horváth R, Cottier K, Pedersen H C and Ramsden J J 2008 Multidepth screening of living cells using optical waveguides *Biosens. Bioelectron.* **24** 805–10

[10] Vollmer F and Arnold S 2008 Whispering-gallery-mode biosensing: label-free detection down to single molecules *Nat. Methods* **5** 591–6

[11] Kashyap R and Nemova G 2009 Surface plasmon resonance-based fiber and planar waveguide sensors *J. Sensors* **2009** 1–9

[12] Ramsden J J and Horvath R 2009 Optical biosensors for cell adhesion *J. Recept. Signal Transduction* **29** 211–23

[13] Ueno H *et al* 2010 Simple dark-field microscopy with nanometer spatial precision and microsecond temporal resolution *Biophys. J.* **98** 2014–23

[14] Enoki S, Iino R, Morone N, Kaihatsu K, Sakakihara S, Kato N and Noji H 2012 Label-free single-particle imaging of the influenza virus by objective-type total internal reflection dark-field microscopy *PLoS One* **7** e49208

[15] Hill D J, Pinion C W, Christesen J D and Cahoon J F 2014 Waveguide scattering microscopy for dark-field imaging and spectroscopy of photonic nanostructures *ACS Photonics* **1** 725–31

[16] Agnarsson B *et al* 2015 Evanescent-light-scattering microscopy for label-free detection: from characterization of single surface-bound lipid vesicles to studies of cell-attachment kinetics *ACS Nano* **9** 11849–62

[17] Axelrod D, Burghardt T P and Thompson N L 1984 Total internal reflection fluorescence *Annu. Rev. Biophys. Bioeng.* **13** 247–68

[18] Tinguely J C, Helle O I and Ahluwalia B S 2017 Silicon nitride waveguide platform for fluorescence microscopy of living cells *Opt. Express* **25** 27678–90

[19] Diekmann R *et al* 2017 Chip-based wide field-of-view nanoscopy *Nat. Photonics* **11** 322–8

[20] Agnarsson B, Ingthorsson S, Gudjonsson T and Leosson K 2009 Evanescent-wave fluorescence microscopy using symmetric planar waveguides *Opt. Express* **17** 5075–82

[21] Hassanzadeh A, Ma H K, Dixon S J and Mittler S 2012 Visualization of the solubilization process of the plasma membrane of a living cell by waveguide evanescent field fluorescence microscopy *J. Biomed. Opt.* **17** 076025

[22] Ramachandran S, Cohen D A, Quist A P and Lal R 2013 High performance, LED powered, waveguide based total internal reflection microscopy *Sci. Rep.* **3** 2133

[23] Thoma F, Langein U and Mittler-Neher S 1997 Waveguide scattering microscopy *Opt. Commun.* **134** 16–20

[24] Hunsperger R G 2009 *Integrated Optics* 6th edn (Berlin: Springer)

[25] Ma H, Jen A K-Y and Dalton L R 2002 Polymer-based optical waveguides: materials, processing, and devices *Adv. Mater.* **14** 1339–65

[26] Agnarsson B, Wayment-Steele H K, Hook F and Kunze A 2016 Monitoring of single and double lipid membrane formation with high spatiotemporal resolution using evanescent light scattering microscopy *Nanoscale* **8** 19219–23

[27] Agnarsson B, Halldorsson J, Arnfinnsdottir N, Ingthorsson S, Gudjonsson T and Leosson K 2010 Fabrication of planar polymer waveguides for evanescent-wave sensing in aqueous environments *Microelectron. Eng.* **87** 56–61

[28] Harold S and Frank W R 1969 Effect of polymer surface morphology on adhesion and adhesive joint strength: II. FEB Teflon and nylon 6 *J. Polym. Sci.* A **7** 105–11

[29] Roberts R, Ryan F, Schonhorn H, Sessler G and West J 1976 Increase of gold-teflon FEP joint strength by removal of deposited aluminum prior to gold deposition for electret applications *J. Appl. Polym. Sci.* **20** 255–65

[30] Vogel S and Schonhorn H 1979 Adhesion of evaporated metallic films onto polyethylene and poly (tetrafluoroethylene): importance of surface crosslinking *J. Appl. Polym. Sci.* **23** 495–501

[31] Adams T M and Layton R A 2010 Creating structures—micromachining *Introductory MEMS: Fabrication and Applications* (Boston, MA: Springer) pp 95–130

[32] Hammer M 2-D mode solver for dielectric multilayer slab waveguides http://computational-photonics.eu/oms.html

[33] Gorin A, Jaouad A, Grondin E, Aimez V and Charette P 2008 Fabrication of silicon nitride waveguides for visible-light using PECVD: a study of the effect of plasma frequency on optical properties *Opt. Express* **16** 13509–16

[34] Halldorsson J, Arnfinnsdottir N B, Jonsdottir A B, Agnarsson B and Leosson K 2010 High index contrast polymer waveguide platform for integrated biophotonics *Opt. Express* **18** 16217–26

[35] Lang E, Baier J and Köhler J 2006 Epifluorescence, confocal and total internal reflection microscopy for single-molecule experiments: a quantitative comparison *J. Microsc.* **222** 118–23

[36] Liu L, Kan A, Leckie C and Hodgkin P D 2016 Comparative evaluation of performance measures for shading correction in time-lapse fluorescence microscopy *J. Microsc.* **266** 15–27

[37] Lundgren A, Agnarsson B, Zirbs R, Zhdanov V P, Reimhult E and Hook F 2016 Nonspecific colloidal-type interaction explains size-dependent specific binding of membrane-targeted nanoparticles *ACS Nano* **10** 9974–82

[38] Lundgren A *et al* 2018 Affinity purification and single-molecule analysis of integral membrane proteins from crude cell-membrane preparations *Nano Lett.* **18** 381–5

[39] Le N C H, Dao D V, Yokokawa R, Wells J and Sugiyama S 2007 Design, simulation and fabrication of a total internal reflection (TIR)-based chip for highly sensitive fluorescent imaging *J. Micromech. Microeng.* **17** 1139–46

[40] Braslavsky I, Amit R, Jaffar Ali B M, Gileadi O, Oppenheim A and Stavans J 2001 Objective-type dark-field illumination for scattering from microbeads *Appl. Opt.* **40** 5650–7

[41] Bu X, Chen H, Gai H, Yang R and Yeung E S 2009 Scattering imaging of single quantum dots with dark-field microscopy *Anal. Chem.* **81** 7507–9

[42] Ambrose W P and Nolan P M G J P 1999 Single-molecule detection with total internal reflection excitation: comparing signal-to-background and total signals in different geometries *Cytometry* **36** 224–31